Journal of Materials Chemistry A

ROYAL SOCIETY OF CHEMISTRY

PAPER

View Article Online
View Journal | View Issue

Cite this: J. Mater. Chem. A, 2025, 13, 33798

Exciton dynamics in planar dumbbell-shaped electron-donor molecules for organic optoelectronics

Jiang Jing, [ab] Emilie Steveler, [af] Amira Mounya Gharbi,[c] Sébastien Marbach,[a] Pascal Didier, [d] Gilles Ulrich,[e] Ibrahim Bulut,[e] Nicolas Leclerc, [e] Wilfried Uhring,[a] Jérémie Léonard, [c] Benoît Heinrich, [e] Patrick Lévêque [a] and Thomas Heiser *[a]

Exciton dynamics play a crucial role in determining the efficiency of organic photovoltaic devices and photo-detectors. However, establishing clear correlations between molecular structure and exciton diffusion length remains a significant challenge, limiting the rational design of more efficient materials. In this study, we investigate exciton transport in thin films of a planar dumbbell-shaped electron donor composed of discotic triazatruxene end-groups and an electron-deficient central unit. These molecules self-assemble into unique bridged-columnar structures, which are known to support efficient charge transport, although their impact on exciton dynamics had not yet been explored. Using a combination of time-resolved photoluminescence (TRPL), spatially resolved TRPL, and exciton–exciton annihilation measurements, we examine how structural order influences exciton diffusion in both the columnar-nematic and crystalline phases. We show that crystallization leads to a twofold increase in exciton diffusion length, reaching values comparable to those observed in state-of-the-art non-fullerene acceptors. Although the molecules exhibit a typical Stokes shift that is not particularly favorable for Förster energy transfer (FRET), efficient exciton transport is nonetheless achieved—enabled by long exciton lifetimes and anisotropic energy transfer within its distinctive bridged-columnar architecture. These results, supported by FRET analysis, highlight the effectiveness of the molecule's tailored dumbbell-shaped design and its ability to self-assemble into ordered structures that support both long-range exciton diffusion and efficient charge mobility.

Received 7th August 2025
Accepted 2nd September 2025

DOI: 10.1039/d5ta06394a

rsc.li/materials-a

1. Introduction

In organic semiconductors, the free charge carrier generation under illumination is generally hindered by large binding energies of the singlet excitons. To overcome this limitation, organic solar cells and photodetectors typically use blends of electron donor (D) and electron acceptor (A) molecules to form a bulk heterojunction (BHJ) that facilitates exciton dissociation at the D/A interface.[1] Achieving BHJs with high quantum efficiencies requires that the size of the donor and acceptor domains be on the order of the exciton diffusion length—under 20 nm in most organic semiconductors.[2,3] Controlling the blend morphology at this nanoscale without compromising charge transport is challenging and narrows considerably the processing window for making high-performance devices.[4] There is thus a strong interest in designing materials (whether donor or acceptor) that simultaneously exhibit long exciton diffusion lengths and efficient charge transport. This is exemplified by the recent success of non-fullerene acceptors (NFAs) in boosting the performances of BHJ solar cells. The exceptionally large exciton diffusion length observed in NFA domains together with their good charge transport properties led to record device efficiencies with acceptor domain sizes up to 45 nm—well beyond the usual limit.[5–7]

Singlet exciton diffusion in organic semiconductors is often modelled as Förster resonant energy transfer (FRET) between neighbouring molecules.[8–10] Within this model, the exciton diffusion coefficient is expected to increase with greater overlap between absorption and emission spectra, shorter intermolecular distances, and reduced structural and energetic disorder. For NFAs, the exceptional excitonic and electronic

[a]Laboratoire des Sciences de l'Ingénieur, de l'Informatique et de l'Imagerie (ICube), 23, Rue Du Loess, 67037 Strasbourg, France. E-mail: thomas.heiser@unistra.fr
[b]Paris Curie Engineering School, Beijing University of Chemical Technology, Beijing 100029, China
[c]Institut de Physique et Chimie des Matériaux de Strasbourg (IPCMS), Université de Strasbourg, CNRS, 23, Rue Du Loess, 67034 Strasbourg, France
[d]Laboratoire de Bioimagerie et Pathologies (LBP), Faculté de Pharmacie, 74 Route Du Rhin, 67401 Illkirch, France
[e]Institut de Chimie et Procédés pour l'Energie, l'Environnement et la Santé (ICPEES), Université de Strasbourg, CNRS, 25 Rue Becquerel, 67087 Strasbourg, France
[f]INSA Strasbourg, 24 Boulevard de la victoire, 67084 Strasbourg Cedex, France

properties were attributed to their rigid conjugated backbones, which result in small Stokes shifts and high structural order.[7,11] Analogously, donor molecules with efficient exciton diffusion and hole transport should improve further the performance of organic solar cells. However, their development is hampered by a lack of chemical design rules. A better understanding of the relationships between molecular structure, molecular self-assembling, exciton diffusion and charge transport is therefore of considerable importance to the field of organic optoelectronic and photovoltaic devices.[5,8,12–15]

In this report, we provide a comprehensive analysis of exciton dynamics in thin films of triazatruxene-based electron-donor molecules, named "TPD_{C8}-TAT_{C8}" (Fig. 1). In a previous report, we have shown that the planar triazatruxene (TAT) end-groups lead to the formation of a distinctive bridged columnar network that facilitates charge transport along three directions.[16,17] In addition, preliminary time-resolved photoluminescence studies of similar TAT derivatives indicated that the exciton lifetime is only weakly impacted by molecular π–π stacking interactions.[18] This unique combination of properties motivated us to investigate further the exciton dynamics in this specific bridged columnar network with the goal to enhance our understanding of the relationship between molecular assembly and exciton transport and identify new design routes for efficient donor molecules.

We investigated exciton dynamics in TPD_{C8}-TAT_{C8} thin films by utilizing conventional time-resolved photoluminescence (or "macro-TRPL") and spatially-resolved TRPL (or "micro-TRPL") measurements. Micro-TRPL investigations help clarify the origin of non-exponential transients observed by conventional macro-TRPL on thin films, whereas exciton–exciton annihilation experiments performed by macro-TRPL enable the determination of exciton diffusion lengths in different solid states. The data are further compared to the exciton diffusion properties obtained by analysing the stationary optical properties of the material within the FRET theory. The results show that the exciton diffusion length increases by a factor of 2 with structural order, reaching 35 nm, close to the highest values reported for NFAs. Together with the previously reported highly efficient 3D charge transport, our findings provide evidence that the bridged-columnar network formed by these dumbbell-shaped molecules enables strong intermolecular coupling without promoting exciton quenching—a combination of properties highly advantageous for organic photovoltaics.

2. Results and discussion

2.1 Material properties and time-resolved photoluminescence

TPD_{C8}-TAT_{C8} molecules are composed of two discotic triazatruxene electron-donating end-units and a central thiophene-thienopyrroledione-thiophene (TPD) electron deficient unit. Both units are functionalized with linear C_8H_{17} alkyl chains to form a highly soluble planar dumbbell-shaped molecule (Fig. 1a). The molecular synthesis as well as the thermal, electronic, photovoltaic (in donor/fullerene blends) and structural properties of TPD_{C8}-TAT_{C8} have been reported previously.[17,18] At room temperature, TPD_{C8}-TAT_{C8} molecules in thin films can be either in a frozen columnar-nematic liquid crystalline state or in a crystalline state, depending on its thermal history. In this work, the annealing conditions were carefully selected to achieve thin films in both states, allowing to investigate the influence of structural disorder on the excitonic properties (see last section for the experimental details). Polarized optical micrographs (POM) and atomic force microscopy (AFM) topography of TPD_{C8}-TAT_{C8} thin films

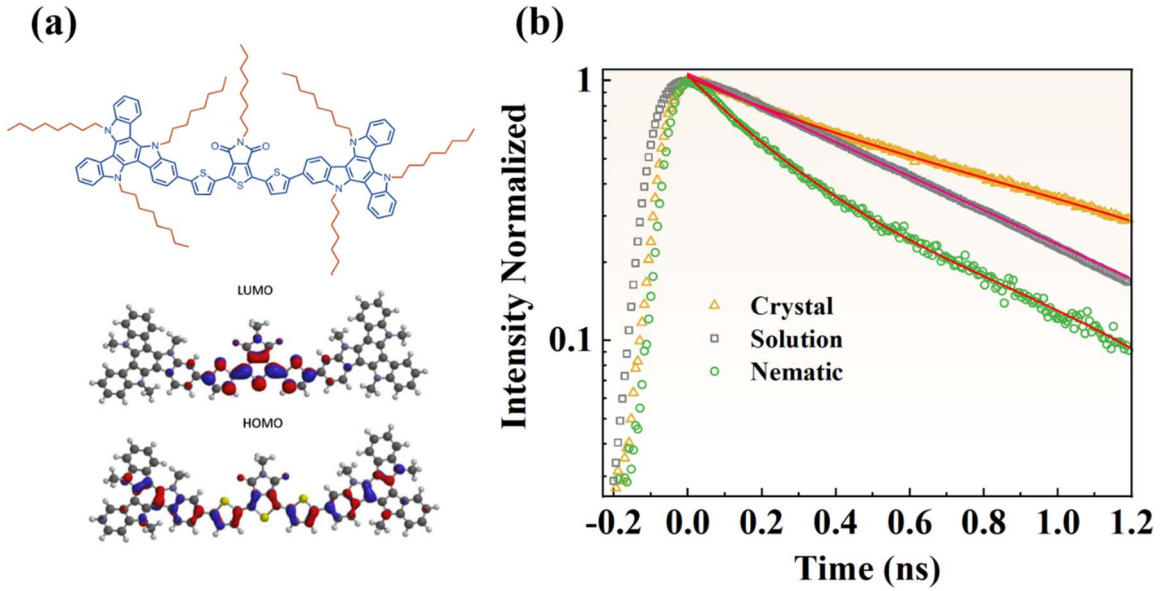

Fig. 1 (a) Chemical structure of TPD_{C8}-TAT_{C8}, and frontier orbitals calculated using density functional theory at the B3LYP/6-311 + G* level in vacuum. The alkyl side-chains were substituted by methyl groups to reduce computation time. (b) Macro-TRPL transients of TPD_{C8}-TAT_{C8} samples (solution and solid states). Solid lines represent exponential fits to the data.

(Fig. S1 and S2) show that the crystallized films consist of a collection of micrometer-sized crystals embedded in a thin structureless TPD_{C8}-TAT_{C8} layer, whereas the frozen liquid-crystalline films are homogeneous and exhibit low surface roughness.

Stationary absorption and continuous wave photoluminescence (CW-PL) spectra of TPD_{C8}-TAT_{C8} thin films are plotted in Fig. S3. In both solid states, the Stokes shift is estimated to 0.25 eV, close to values commonly observed in other organic semiconductors, but larger than those of NFAs.[19] As a consequence, the spectral overlap between absorption and emission is rather moderate and not expected to specifically favour exciton diffusion.

The PL transients measured on TPD_{C8}-TAT_{C8} in solution and in thin films by macro-TRPL are shown in Fig. 1b. In solution, the PL transient follows a mono-exponential decay with a 0.7 ns decay time, whereas in thin films, the decays are non-exponential. The photoluminescence (PL) transients can be accurately fitted using double-exponential functions, with the corresponding parameters summarized in Table 1. Notably, reducing the laser intensity does not alter the shape of the PL decay (Fig. S9), thereby ruling out any significant contribution from exciton–exciton annihilation to the observed non-exponential behavior.[10] It is also worth noting that exciton decay occurs more slowly in the crystalline film than in solution.

2.2 Micro-TRPL measurements

To clarify the origin of the non-exponential decays, we performed additional micro-TRPL on both films. In micro-TRPL, a pulsed 950 nm laser beam, 300 nm in diameter, is scanned over the sample surface, generating excitons by two photon absorption. The PL transients are measured at each point across the sample, creating a spatially resolved map of PL decay times. Remarkably, unlike macro-TRPL transients, the micro-TRPL transients follow single exponential decays (Fig. 2), with decay-times (τ_{PL}) that vary across the sample and between samples. The τ_{PL} map of a typical crystallized film is shown in Fig. 2a. The highest τ_{PL} values are observed on the crystal, whereas lower and more scattered values are found in the surrounding area. In the latter, the significant scattering arises from the low surface density of fluorescent molecules, leading to a correspondingly large error margin of the decay time. The decay-time histogram of the mapped area (Fig. 2c) displays two more or less narrow distributions centered respectively at 1.07 $\pm$ 0.10 ns and 0.45 $\pm$ 0.20 ns. The former value corresponds to measurements done on the crystal and aligns well with the longer decay time observed in the crystalline film by macro-TRPL (Table 1).

The micro-TRPL map performed on the columnar-nematic film is shown in Fig. 2b. It reveals the existence of domains with rather uniform decay-times, separated by dark areas for which the signal-to-noise ratio was too low to estimate decay-times. Since the film topography shows no signs of molecular de-wetting (Fig. S1 and S2), we tentatively attribute the low intensity PL areas to liquid-crystal domains where the local average orientation of molecules is such that their transition dipole is nearly perpendicular to the excitation light polarization axis. A remarkably narrow decay time distribution, centered at 0.45 ns $\pm$ 0.05 ns, is observed on this sample (Fig. 2d). This value agrees well with those measured in areas surrounding the crystal in the crystallized film (low lifetime distribution in 2c).

The micro-TRPL results suggest that the double exponential form of the macro-TRPL transients measured on the crystalline film arises from the coexistence of crystalline and columnar-nematic domains. Indeed, the 1.07 ns lifetime observed on the crystal agrees well with the longer time constant measured by macro-TRPL. It is worth noting that the histograms in Fig. 2 display the number of pixels per lifetime value and are not representative for the contribution of each decay time to the macro-PL transient amplitude. Moreover, the micro-TRPL lifetimes measured in the nematic film (Fig. 2d) and in the nematic domains of the crystalline film (Fig. 2c) are close to the average time constant (defined by $A_1\tau_1 + A_2\tau_2$) measured by macro-TRPL on the nematic film. Intriguingly, the lifetime distribution shown in Fig. 2d is much narrower than the difference between the nematic lifetimes measured by micro-TRPL (0.45 ns) and macro-TRPL (0.15–0.20 ns). This discrepancy may be the consequence of the difference in size of the areas probed by both techniques ($\sim$3 mm^2 *vs.* 2500 μm^2), provided the decay time changes over a length scale comparable or larger than the area probed by micro-TRPL, but smaller than that of macro-TRPL. In this case, the contribution of different decay rates to the macro-TRPL signal would result in non-exponential transients, while mono-exponential decays with a narrow lifetime distribution would be observed in micro-TRPL.

To verify this assertion, we performed additional micro-TRPL measurements on separate areas of the same columnar-nematic film. As shown in Fig. S4, the PL transients always decay mono-exponentially, but the decay time constants vary significantly over the cumulated scanned area. The decay time histogram cumulating six mapped areas (Fig. S4) reveal three narrow gaussian distributions centered around (0.45 $\pm$ 0.03) ns (0.55 $\pm$ 0.06) ns and (0.64 $\pm$ 0.04) ns, respectively. The PL map clearly indicates that each gaussian distribution arise from a specific region in the film (different colors in Fig. S4). Similarly, micro-TRPL maps done on different areas of the crystalline film confirm the mono-exponential shape of PL transients on the crystals (Fig. S5), but the decay-times vary among crystals and in some cases reach values as high as 1.3 ns. The decay-time

Table 1 Fitting parameters used to adjust macro-TRPL transients with mono or double-exponential decays. The fits were realized after deconvoluting the TRPL transients with the impulse response function of our set-up

	Thin film ($A_1\ e^{-t/\tau_1} + A_2\ e^{-t/\tau_2}$)	
Solution ($A\ e^{-t/\tau}$)	Columnar-nematic	Crystalline
0.70 $\pm$ 0.05 ns	$\tau_1 = 0.15 \pm 0.05$ ns	$\tau_1 = 0.20 \pm 0.05$ ns
	$\tau_2 = 0.60 \pm 0.05$ ns	$\tau_2 = 1.10 \pm 0.05$ ns
	$A_1 = 0.40 \pm 0.02$	$A_1 = 0.10 \pm 0.02$
	$A_2 = 0.60 \pm 0.02$	$A_2 = 0.90 \pm 0.02$

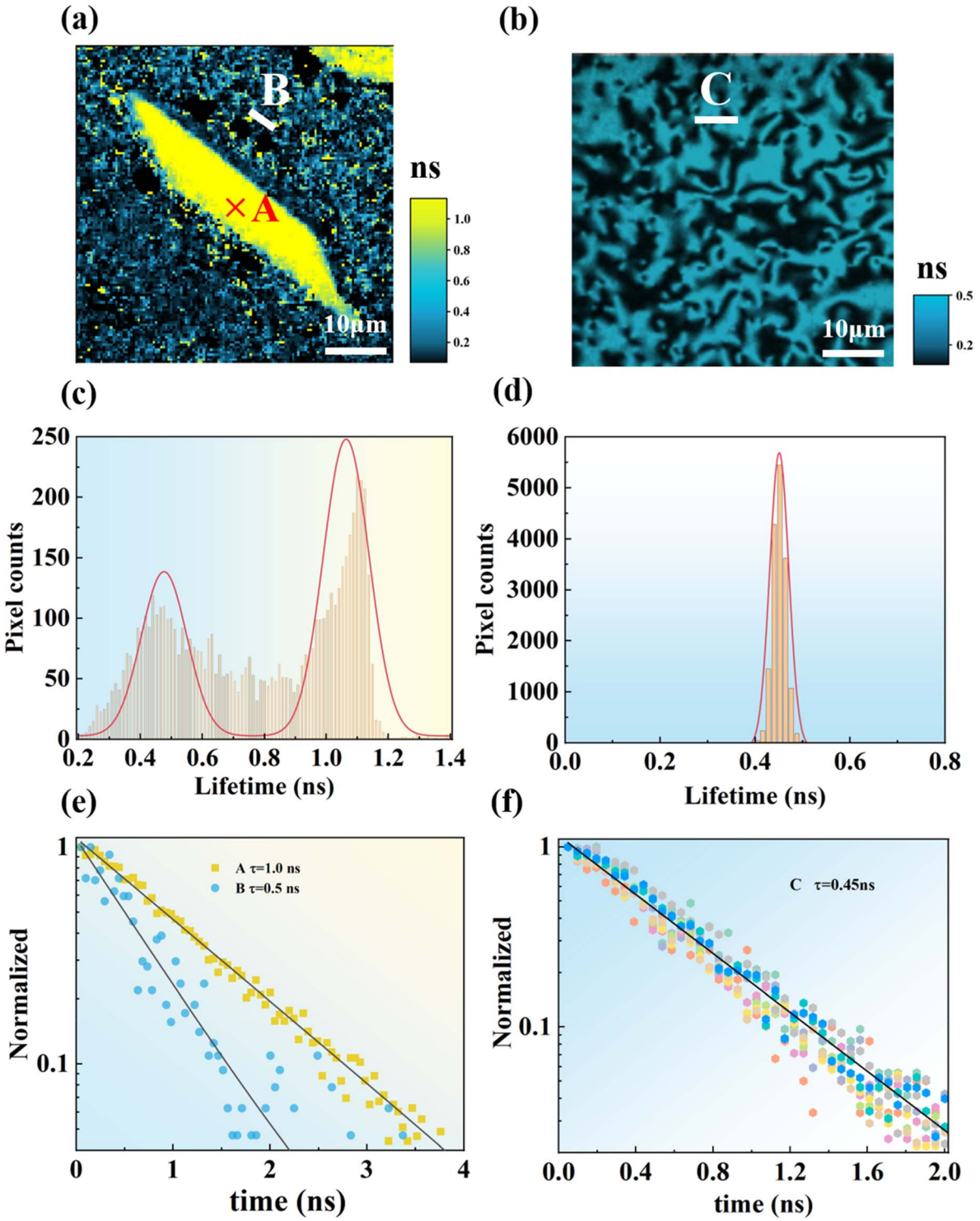

Fig. 2 Micro-TRPL map of exciton lifetimes in (a) crystallized and (b) columnar-nematic film of TPD_{C8}-TAT_{C8}. The figure (c) and (d) represent the decay-time histogram over the 50 × 50 μm mapped area of (a) and (b). (e) TRPL transients measured at point A or averaged over line B in (a), with mono-exponential fits (solid lines). (f) TRPL transients measured along line C in (b), with mono-exponential fit (solid line). Data points associated with a specific transient are distinguished by color.

histogram cumulating six different areas in the crystalline film displays two narrow gaussian distributions, centered around (1.03 ± 0.13) ns and (1.30 ± 0.09) ns, respectively. The broader distribution seen at lower decay-times originates from the residual nematic domains between crystals.

Interestingly, on the crystal with the highest exciton lifetime, a decrease in decay time can be seen near the edges of the

crystal (yellowish borderline, Fig. S5), whereas this effect is absent in the crystal with the lower exciton lifetime. Highly anisotropic exciton diffusion along the crystal axes, coupled with efficient quenching near the crystal surfaces, could possibly be at the origin of this behavior. Indeed, if the slow exciton diffusion axis is perpendicular to the illuminated surface and the fast diffusion axis lies parallel to it, fewer excitons will reach the crystal surface to be quenched compared to the opposite configuration. As a result, the observed exciton decay time will be longer. Furthermore, exciton quenching is expected to be more pronounced near the crystal's lateral facets, leading to a reduced exciton lifetime – consistent with the experimental observations shown in Fig. S5. In other words, the variations in exciton lifetime distributions observed in Fig. S5 may result from anisotropic exciton diffusion and reflect differences in crystal orientation within the sample.

The observation of local variations in exciton lifetimes in the columnar nematic film is more intriguing, since the changes occur on a length scale significantly larger than the typical structural correlation lengths in a mesophase. A possible explanation could be local variations in the exciton quenching efficiency of the surface due to possible surface contaminants, though this has yet to be confirmed. For the following, we will consider that the time constants obtained from the double-exponential fits of macro-TRPL transients are representative of the dominant mono-exponential decay rates occurring in the film, regardless of the underlying mechanisms. Therefore, the exciton lifetime in TPD_{C8}-TAT_{C8} crystals will be described by $\tau_{ex,c} = (1.1 \pm 0.2)$ ns, the long decay time measured by macro-TRPL (Table 1). For the columnar nematic phase, the exciton lifetime has been found by micro-TRPL to vary locally between 0.20 and 0.65 ns, which is consistent with the decay rates estimated from the double-exponential fit of macro-TRPL transients (Table 1). The average macro-TRPL decay time (defined by $A_1\tau_1 + A_2\tau_2$) is therefore a good approximate of the exciton lifetime in the nematic phase. Correspondingly, the exciton

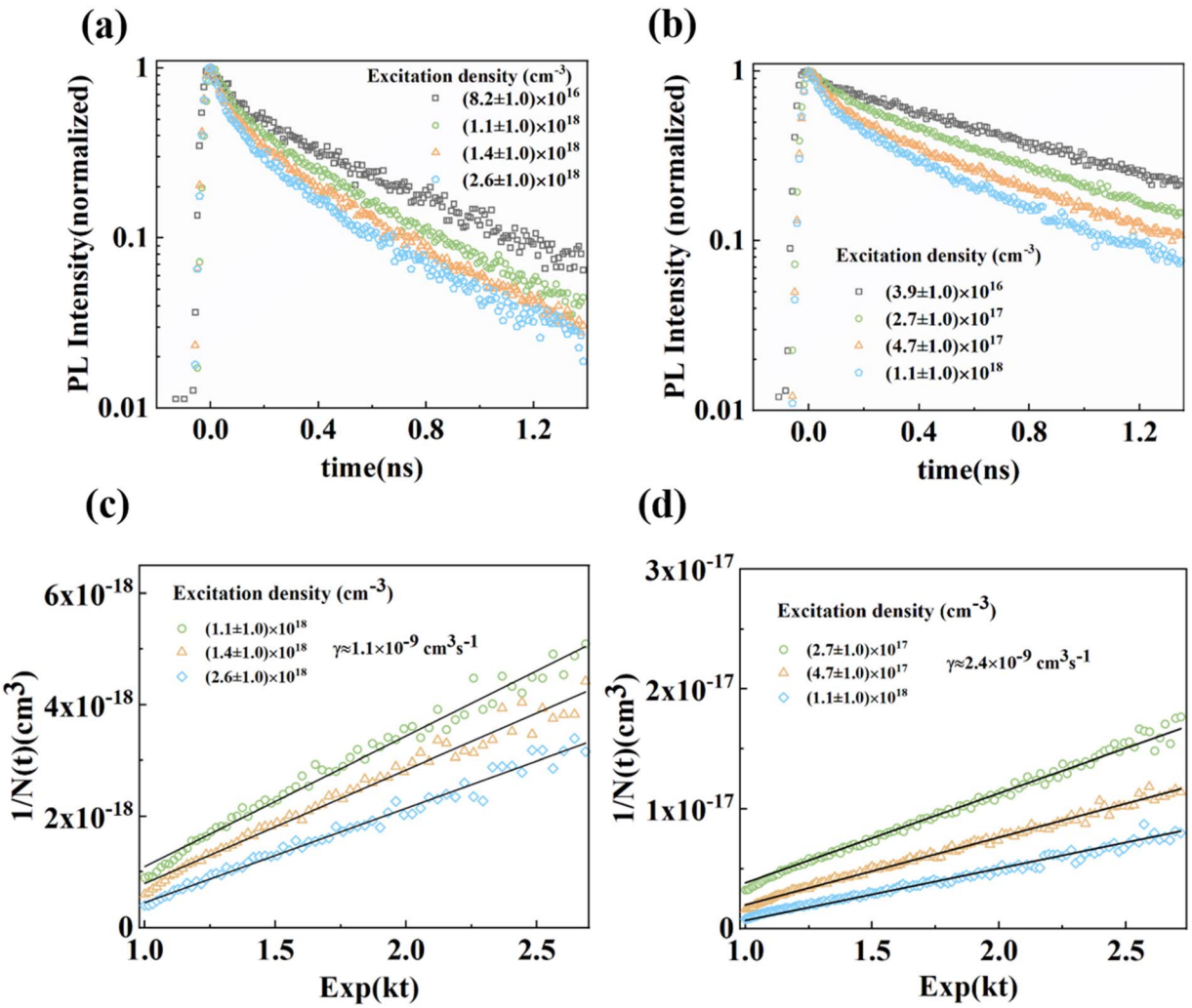

Fig. 3 Normalized time-resolved photoluminescence transients on TPD_{C8}-TAT_{C8} thin films in the nematic state (a) and the crystalline state (b). EEA data replotted as $\frac{1}{N(t)}$ *versus* e^{kt}, using $k = 2.5 \times 10^9$ s^{-1} for the nematic state (c) and $k = 9.1 \times 10^8$ s^{-1} for the crystalline state (d), and the maximum PL position as time origin. The straight lines are least-square fits to eqn (3) using γ as single fitting parameter. The coefficients of determination are 0.967 and 0.978 for (c) and (d), respectively.

lifetime in the nematic film will be described by $\tau_{ex,n} = (0.4 \pm 0.2)$ ns. The smaller decay time can be attributed to the residual nematic domains in the film. Note that in the crystalline film, the amplitude ratio between the two exponential components indicates that the residual columnar nematic phase accounts for approximately 10% of the total film.

2.3 Exciton diffusion coefficient estimated by exciton–exciton annihilation

Measuring macro-TRPL transients as a function of laser beam intensity is a well-known method to estimate exciton diffusion coefficients in organic semiconductors.[20] It assumes that the rate of exciton–exciton annihilation (EEA) is limited by exciton diffusion, leading to an effective exciton lifetime that decreases with increasing exciton density. The resulting time-dependent PL intensity is proportional to the exciton density, N(t), which can be described by the following equation:[21]

$$\frac{dN(t)}{dt} = G - kN(t) - \gamma N(t)^2 \quad (1)$$

where G is the average exciton generation rate, k the exciton decay rate in the absence of EEA, and γ the exciton–exciton annihilation rate. The latter is given by $\gamma = 4\pi R_a D\left(1 + \frac{R_a}{\sqrt{2\pi Dt}}\right)$[22] with D the exciton diffusion coefficient and R_a the annihilation radius. The value of R_a is difficult to evaluate and is often taken equal to 1 nm.[21,23,24] We use the same assumption to analyze our data.

At times larger than $\frac{{R_a}^2}{2\pi D}$ (which corresponds to less than 20 ps for $D = 10^{-4}$ cm^{2}s^{-1}), the annihilation rate reduces to $\gamma \approx 4\pi R_a D$ and eqn (1) can be solved analytically by:[25]

$$\frac{1}{N(t)} = \left(\frac{1}{N(0)} + \frac{\gamma}{k}\right)\exp(kt) - \frac{\gamma}{k} \quad (2)$$

with $N(0)$ the initial number of excitons per unit volume. $N(0)$ can be approximated by $\frac{E_p}{V}\frac{\lambda}{hc}(1 - 10^{-A})$, with E_p the laser pulse energy, V the excited volume, λ the excitation wavelength (515 nm), A the absorbance of the film at λ, h Planck's constant, and c the speed of light in vacuum. V is commonly taken equal to the beam section (S) times the sample thickness (W), neglecting the impact of the non-uniform incident light intensity. Although this simplified procedure has recently been shown to lead to an under-estimation of the annihilation rate (and hence of D),[26] we kept using it in this study as it facilitates comparison with literature data and should not affect the main conclusions of our study. Accordingly, we estimated S, W and A to, respectively, 5.8×10^{-7} cm^2, (100 ± 10) nm, and 0.2 for the nematic film, and to 13.7×10^{-7} cm^2, (250 ± 10) nm and 0.3 for the crystalline film (Fig. S6 and Table S1).

The PL transients measured at room temperature at different laser powers on columnar-nematic and crystallized thin films are shown in Fig. 3a and b. In Fig. 3c and d the same data is re-plotted as $\frac{1}{N(t)}$ *versus* e^{kt}, with the time origin fixed at the maximum photoluminescence intensity and using $k = \frac{1}{\tau_{ex,n}}$ for the columnar-nematic film and $k = \frac{1}{\tau_{ex,c}}$ for the crystalline film. The straight lines are least-square fits to eqn (2) with γ as single fitting parameter. TRPL transients measured at the lowest laser power are shown separately in Fig. S7 to avoid broadening of the vertical axis in Fig. 3c. The fitting quality is excellent for both, the nematic and the crystalline samples.

The γ values estimated for both states and the corresponding diffusion coefficients (D) are summarized in Table 2. Notably, γ is significantly larger in the crystalline film compared to the columnar-nematic film. Consequently, the exciton diffusion length in 3D, defined as $L_{ex} = \sqrt{2ZD\tau_{ex}}$ with $Z = 3$ and τ_{ex} the exciton lifetime,[10,27] increases by more than a factor of two, reaching 35 nm in the crystalline film. This value is close to those reported for NFAs, despite the larger Stokes shift for TPD_{C8}-TAT_{C8} and previously reported strong π–π stacking interactions.[15] This remarkable finding can be attributed to the longer exciton lifetime in TPD_{C8}-TAT_{C8} crystals and is likely a consequence of the distinctive bridged columnar molecular network.

2.4 Analysis of exciton dynamics based on Förster resonant energy transfer

Another commonly used method to estimate exciton diffusion coefficients in molecular thin films relies on FRET theory.

Table 2 Exciton diffusion parameters estimated by EEA and FRET theory

Parameters		In solution	Columnar-nematic state	Crystalline state
Exciton lifetime (ns)		0.70 ± 0.05	$\tau_{ex,n} = 0.42 \pm 0.20$	$\tau_{ex,c} = 1.1 \pm 0.2$
EEA	γ (cm^3 s^{-1})	—	$(1.1 \pm 1.0) \times 10^{-9}$	$(2.4 \pm 2.0) \times 10^{-9}$
	D (cm^2 s^{-1})[a]		8.5×10^{-4}	1.9×10^{-3}
	L_{3D} (nm)[a]		14	35
FRET theory	ϕ_L (%)	14.0 ± 1.0	2.5 ± 0.5	5.2 ± 1.0
	J (nm^4 M^{-1} cm^{-1})	—	$(0.9 \pm 0.2) \times 10^{14}$	$(2.6 \pm 0.2) \times 10^{14}$
	n		1.55 ± 0.05	1.74 ± 0.10
	k_{tr} (s^{-1})		$(5 \pm 1) \times 10^{12}$	$(6 \pm 1) \times 10^{12}$
	D (cm^2 s^{-1})[a]		1.2×10^{-3}	1.6×10^{-3}
	L_{3D} (nm)[a]		17	30

[a] While the ratio between γ values – and hence the diffusion coefficients D – is a clear outcome of the comparison between nematic and crystalline states, the uncertainty on the absolute values is estimated to be approximately 50% for D and 30% for L_{3D}.

The FRET theoretical framework is based on the point dipole approximation, which is best suited if the distance between the energy donor and acceptor molecules is larger than the size of the individual molecules. This condition may not be met in case of densely packed large molecules, such as TPD_{C8}-TAT_{C8}. Despite this limitation, the method remains widely used as it gives easy access to an estimate of D from conventional steady-state optical measurements.[10] For completeness and to enable comparison with literature data, we incorporated this method into our study.

According to FRET theory, the energy transfer between molecules is given by:[21,28,29]

$$k_{tr} = \left[\frac{9000(\ln\ 10)\kappa^2\phi_L}{128\ \pi^5 n^4 N_A \tau_{ex} r^6} J\right] \quad (3)$$

where $J = \int_0^\infty F(\lambda)\varepsilon(\lambda)\lambda^4 d\lambda$ is the spectral overlap between normalized fluorescence intensity $F(\lambda)$ (area normalized to unity) and molar extinction coefficient $\varepsilon(\lambda)$ (M^{-1} cm^{-1}), κ^2 the dipole moment orientation factor, r the distance between energy donor and energy acceptor, ϕ_L and τ_{ex} the donor fluorescence quantum yield and exciton decay time respectively, n the refractive index of the medium, averaged over the measured wavelength range, and N_A Avogrado's number. Notice here that donor and acceptor are two (nearby) molecules of identical nature; we may refer to such energy transfer as "homo-FRET".

The experimental $\varepsilon(\lambda)$ values of TPD_{C8}-TAT_{C8} in both nematic and crystalline states were determined using standard spectrophotometry. The J value was calculated based on the absorption and emission spectra shown in Fig. S3, with further details provided in Section 4. The refractive index n of the nematic film was measured by ellipsometry. On the other hand, for the crystalline film, n was estimated by measuring the reflectance R of isolated crystals by white-light interference microscopy[30] (Fig. S8b) and applying $R = \left[\frac{n-1}{n+1}\right]^2$. The fluorescence quantum yields were measured by spectrofluorometer. For the latter measurements, thin films were spin coated on a circular quartz substrate and annealed to achieve either columnar-nematic or crystalline states. The results are summarized in Table 2 (more details are given in Section 4).

Since k_{tr} decreases with r^{-6}, it is mostly dependent on the orientational and structural order at short distances. Previous structural investigations of the TPD_{C8}-TAT_{C8} mesophase[17] have shown that the molecules self-assemble into a bridged hexagonal-columnar structure, with the columns formed by the stacking of TAT end-units (Scheme S1). In this structure, each TPD_{C8}-TAT_{C8} molecule participates to two neighboring columns. The assembly is preserved over about 3–3.5 nm along the columns and about 7 nm perpendicular to the columns, representing 8–9 molecules in the piling direction and 4 columns in the lateral direction. The probability P_0 for two nearest neighbor molecules to belong to the same two columns, and thus be oriented parallel to each other, should be approximately $\frac{1}{6}$. Nearest neighbors sharing only one column form angles of either $\pi/3$, $2\pi/3$ and π between each other (see Scheme S1). These angles lead to dipole orientation factors of $\kappa^2 \approx 0.45$, 1.6 and 4 (neglecting the displacement parallel to the columns), while for parallel-oriented molecules, $\kappa^2 = 1$. The parallel-oriented neighboring molecules are separated by the π–π stacking distance ($d_\pi = 0.38$ nm). In contrast, for non-parallel oriented neighboring molecules, the distance between the centers of neighboring molecules is given, approximately, by $L \sin\theta/2$, where $L = 2.2$ nm (see Scheme S1). This leads to distances of 1.1 nm, 1.9 nm or 2.2 nm for $\theta = \pi/3$, $2\pi/3$ and π, respectively, much larger than d_π. The resulting energy transfer rates are thus at least three orders of magnitude lower than that between parallel-oriented molecules. Exciton diffusion is therefore expected to be highly anisotropic. Note that parallel-oriented next-nearest-neighbor molecules may also occur, but with intermolecular distances of $2d_\pi$. The transfer rate between such molecules is 64 times lower than that between nearest neighbor parallel-oriented molecules and contributes only marginally to the overall energy transfer rate along the columnar direction. Based on the above, the average energy transfer rate $\langle k_{tr}\rangle$ in the columnar-nematic phase can be expressed as follows:

$$\langle k_{tr}\rangle = P_0 k_{tr}(r = d_\pi, \kappa^2 = 1) + (1 - P_0) k_{tr}(r \gg d_\pi)$$

$$\approx \frac{1}{6} k_{tr}(r = d_\pi, \kappa^2 = 1) \quad (4)$$

with $k_{tr}(r, \kappa^2)$ given by eqn (3).

The average diffusion coefficient in anisotropic columnar-hexagonal mesophases is given by,[31,32] $D = \frac{1}{3}(D_\parallel + 2D_\perp)$ where $D_\parallel$ and $D_\perp$ are the diffusion coefficients parallel and perpendicular to the columnar direction, respectively. Since the energy transfer rate is predominately along the columnar direction, D can be approximated by:[33]

$$D \approx \frac{1}{3} D_\parallel \approx \frac{1}{6} d_\pi{}^2 \langle k_{tr}\rangle \quad (5)$$

The energy transfer rate and diffusion coefficient calculated using eqn (3)–(5), as well as the resulting diffusion length, are summarized in Table 2. The results are close to those obtained by EEA on the nematic film, despite the fundamentally different approach.

For the crystalline state, the analysis is hampered by the still incomplete knowledge of the crystalline structure. Indeed, previous structural and charge transport investigations[17] allowed only to conclude that the molecules self-assemble into a slightly distorted hexagonal lattice, derived from the parent bridged-columnar nematic mesophase. Nevertheless, given the close relationship between the mesophase and the crystalline phase, we can assume that energy transfer in the crystalline state also occurs predominantly between parallel-oriented molecules, along the columnar direction. Under this assumption, eqn (4) and (5) still apply, although d_π might be slightly reduced in the crystalline state. The energy transfer rate and diffusion coefficients, obtained using $d_\pi = 0.38$ nm, are summarized in Table 2. The diffusion coefficient is found to be

higher than in the mesophase, which is consistent with the EEA data and confirms the impact of structural order on exciton dynamics. However, the variation is less pronounced than that determined by EEA. This discrepancy may partly arise from neglecting a possible reduction in d_π during the nematic-to-crystalline transition.

3. Discussion and conclusion

The diffusion parameters obtained from FRET theory match those derived from EEA, which is quite remarkable given the different approximations on which both methods rely. It should be emphasized that while the absolute values carry significant uncertainty—estimated at about 50% for D and 30% for L_{3D}—the ratio of the γ values, and thus the diffusion coefficients D is a robust result when comparing the nematic and crystalline states. Both data sets follow the same trend and reveal a large impact of the structural order on exciton diffusion: the diffusion coefficient increases by a factor of 2.0 ± 0.4 as the material transitions from the frozen liquid-crystalline state to the more ordered crystalline state. These findings align well with the report of Z. Li *et al.*,[34] who found a strong influence of structural disorder on exciton diffusivity in a donor–acceptor–donor type conjugated molecule, alike that of TPD_{C8}-TAT_{C8}, by using first-principles simulations.[17]

Another remarkable result is the observed increase in exciton lifetime with structural order. Combined with the increase in diffusion coefficient, this feature results in an exciton diffusion length comparable to that observed in non-fullerene acceptors. The long exciton lifetime in the crystalline state is particularly surprising considering the strong intermolecular coupling, as evidenced by the previously reported high hole mobility. Intermolecular coupling promotes phonon-assisted non-radiative recombination and is generally found to reduce the exciton lifetime. We tentatively attribute this property to the bridged columnar molecular structure found in TPD_{C8}-TAT_{C8} crystals. In such an assembly, intermolecular interactions are dominated by the planar TAT-end groups, leaving the central TPD unit surrounded mostly by alkyl-chains. Density functional theory calculations (Fig. 1a) show that the LUMO level in these donor–acceptor–donor molecules is localized on the central TPD unit, while the HOMO level is delocalized over most of the conjugated backbone. Electrons in the excited state may therefore be only weakly coupled to neighboring molecules, avoiding non-radiative recombination pathways. On the other hand, since coupling between the TAT end-groups predominantly affects the HOMO levels, hole transfer proceeds efficiently, as observed experimentally.[16] It is worth mentioning, that a similar end-group-driven molecular self-assembly was reported for A–D–A type non-fullerene acceptors and found to underly the good photovoltaic performance of NFA based solar cells.[5]

As mentioned above, the efficient exciton transport observed in TPD_{C8}-TAT_{C8} contrasts with its large Stokes shift, which is expected to hinder FRET. In our case, this effect appears to be counterbalanced by the higher exciton lifetime. We therefore conjecture that similar triazatruxene-based dumbbell-shaped molecules, incorporating a more rigid linkage between the TAT units and the central core, could benefit from both a reduced Stokes shift—enhancing dipolar coupling—and long exciton lifetimes, potentially enabling access to even greater exciton diffusion lengths.

In summary, we have investigated the exciton diffusion length in planar dumbbell-shaped small molecules, TPD_{C8}-TAT_{C8}, based on discotic electron-rich end-units and an electron-deficient central unit, using time-resolved photoluminescence and photoluminescence quantum yield measurements. Spatially-resolved TRPL experiments proved especially valuable in elucidating the origin of the non-exponential transients observed in conventional TRPL measurements. Exciton–exciton annihilation experiments and quantum yield measurements analyzed as Förster resonant energy transfer, were used to determine the exciton diffusion length in both solid states. Both methods gave rise to similar trends, showing a significant increase of the exciton diffusion coefficient structural order. The resulting highest exciton diffusion length approaches the values observed in NFAs and are likely an outcome of the bridged-columnar self-assembly of the planar dumbbell-shaped molecules. This molecular design shows strong promise for organic electronic applications requiring long exciton diffusion lengths.

4. Experimental

4.1 Molecular synthesis

Synthesis and molecular characterizations of the TPD_{C8}-TAT_{C8} are identical to the procedures described in ref. 17.

4.2 Thin-film deposition conditions and thermal processes

Quartz substrates were used for all samples. The substrates were cleaned with liquid dish soap and sonicated in a series of deionized water, acetone, and isopropanol for 15 minutes each. Next, the substrates were treated by UV-Ozone reactor for 30 minutes to eliminate any organic residues on the surface before spin-coating. All solutions and thin-film depositions were done in a nitrogen-filled glove box. The solutions were prepared with concentrations of 20 mg mL^{-1} in chloroform and stirred overnight at room temperature. Solutions were spun onto clean substrates with a deposition volume of 120 μL and a spin rate of 1500 rpm during 60 seconds. Different annealing steps were applied under nitrogen ambient to achieve the desired solid states:

(I) Nematic state: annealing at 180 °C for 5 seconds (isotropic phase), followed by rapid cooling to room temperature (Fig. S1a).

(II) Crystalline state: annealing at 180 °C for 5 minutes, followed by rapid cooling to room temperature and subsequent gradual heating to 145 °C for 40 minutes (Fig. S1b).

4.3 Continuous-wave photoluminescence

The samples were exposed to a pulsed Nd-YAG laser (355 nm) at a power of 88 mW, and a pulse width at half maximum (FWHM) of 12.5 ns, at a frequency of 15 000 Hz. A BRC112E CCD camera was used as spectrometer.

4.4 Low-intensity macroscopic time-resolved photoluminescence (TRPL)

The TRPL measurements were carried out in atmospheric environment at room temperature. The samples were excited at a wavelength of 511 nm using a laser from AUREA PIXEA-510. The beam characteristics are the following: pulse duration = 90 ps, energy per pulse = 0.05 nJ, a repetition rate = 20 MHz, beam diameter ≈ 2 mm. TRPL was measured using a Hamamatsu C6860 streak camera with a S-20 photocathode in synchro-scan mode. The FWHM of the instrument response function (IRF) is 40 ps.

4.5 Micro-TRPL

Lifetime Imaging Microscopy was performed with a home-made multi-photon laser scanning microscope using a tunable femtosecond laser (Insight DeepSee Spectra Physics) that produces 120 fs pulses at 950 nm with a beam diameter about 300 nm. A 60X 1.2NA water immersion objective was used. The laser power was adjusted to give count rates with peaks up to as few as 10^6 photons per s, so that the pile-up effect can be neglected. Imaging was carried out with a laser scanning system using two fast galvo mirrors (Model 6210, Cambridge Technology), operating in the descanned fluorescence collection mode. The fluorescence was directed to a fiber coupled APD (SPCM-AQR-14-FC, PerkinElmer), which was connected to a time-correlated single photon counting (TCSPC) module (SPC830, Becker & Hickl), operated in the reversed start-stop mode. Typically, the samples were scanned continuously for about 30 s to achieve appropriate photon statistics to analyze the fluorescence decays. Each measurement point resulted in a fluorescence decay which was fitted by a decreasing mono-exponential function.

4.6 Optical absorption measurements

Absorption spectra in thin films were recorded on a Shimadzu UV-2600 spectrophotometer. Molar extinction coefficient (ε in M^{-1} cm^{-1}) is given by

$$\varepsilon = \frac{A}{cl}$$

Where A is the absorbance, l the optical path length and c the molar concentration. In this article, for thin films measurements, we assumed that the optical path length is equal to the film thickness. The molar concentration c is given by:[20]

$$c = 1000\frac{\rho}{M_n}$$

Where ρ is the density of thin films and M_n is the molecular weight of a chromophore. In this article, ρ is 1.11 g cm^{-3} and M_n is 1789.65 g mol^{-1} for the TPD_{C8}-TAT_{C8} bulk material.

4.7 Ellipsometry measurements

Refractive index (n) was obtained by using spectral ellipsometry TN01, HORIBA. The thin films were spin coated on a quartz substrate and annealed according to the description given above.

4.8 White light interference microscopy

The White Light Interference Microscopy set-up is home-built, with details given in a previous published paper.[35] The light source is a white LED Thorlabs MBB1L3. The sample is placed on a piezo electric translator. Three samples of isolated crystals were measured for three different areas (as shown in Fig. S8). The value of n is obtained according to the equation $R = \left[\frac{n-1}{n+1}\right]^2$, and assuming there is no absorption factor.

4.9 Time-resolved photoluminescence for EEA measurements

The EEA measurements were done in atmospheric environment at room temperature using an experimental set-up described in detail elsewhere.[26] Samples were encapsulated to prevent laser enhanced oxidative damage. The sample encapsulation was done in a glove box filled with N_2. The laser wavelength was 515 nm with ~300 fs pulses and a repetition rate ranging from 0.1 to 100 kHz. The excitation energy was 0.4 μJ per pulse at maximum, adjusted with a neutral density filter. The laser beam is focused on the thin film samples by a microscope objective. The beam radius was defined as the root mean square (RMS) width of a Gaussian function obtained by a least-square fit of the PL intensity profile, measured by a digital camera for a fixed beam position (Fig. S6). We obtained ≈6.6 μm for the crystalline sample and ≈4.3 μm for the nematic sample. The TRPL transients were measured using a Hamamatsu C10627 streak camera. The FWHM of the streak camera response function was 20 ps. The repetition rate of the laser was also decreased while gradually increasing the excitation energy (per pulse) to avoid photobleaching of the samples. To verify the absence of photobleaching during the EEA measurements, the TRPL curves were measured a second time at low energy after each excitation at high energy and superimposed with the first measurements.

4.10 Quantum yield

Quantum yields were measured by a FluoroMax®-4 – Spectrofluorometer from HORIBA Scientific, using an integration sphere. The thin films were spin coated on a circular quartz substrate and annealed according to the description given above, circular quartz substrate was used as blank in the sphere.

Author contributions

J. Jing: writing original draft, investigation, data curation. E. Steveler: investigation, methodology, data curation, resources. A. M. Gharbi: investigation. S. Marbach: investigation. P. Didier: methodology. G. Ulrich: methodology. I. Bulut: investigation. N. Leclerc: methodology. W. Uhring: methodology. J. Léonard: investigation. B. Heinrich: formal analysis. P. Lévêque: DFT calculations. T. Heiser: conceptualization, writing – review & editing, resources, supervision.

Conflicts of interest

There are no conflicts to declare.

Data availability

The data that support the findings of this study are available in the SI of this article. See DOI: **https://doi.org/10.1039/d5ta06394a**.

Acknowledgements

The authors gratefully acknowledge the C^3-Fab (ICube) platform for access to the equipment and Yaochen Lin for his critical reading of the manuscript. J. Jing acknowledges financial support from China Scholarship Council (CSC) and the Fundamental Research Funds for the Central Universities (JD2514 and BH202550). AMG and JL acknowledge support from the Region Grand-Est (contract #19-GE6-161), the French ANR *via* the "LHnanoMat" project (ANR-19-CE090006-02), and from the Interdisciplinary Thematic Institute QMat as part of the ITI 2021-2028 program of the University of Strasbourg, CNRS and Inserm *via* the IdEx Unistra (ANR 10 IDEX 0002), SFRI STRAT'US (ANR 20 SFRI 0012), and Labex NIE (ANR-11-LABX-0058-NIE) projects of the French Investments for the Future Program.

References

1 Y. Zou and R. J. Holmes, *Adv. Energy Mater.*, 2015, **5**, 1500019.
2 M. T. Sajjad, A. Ruseckas and I. D. W. Samuel, *Matter*, 2020, **3**, 341–354.
3 S. Giannini, W.-T. Peng, L. Cupellini, D. Padula, A. Carof and J. Blumberger, *Nat. Commun.*, 2022, **13**, 2755.
4 Y. Li, T. Li and Y. Lin, *Mater. Chem. Front.*, 2021, **5**, 2907–2930.
5 L. Ye, K. Weng, J. Xu, X. Du, S. Chandrabose, K. Chen, J. Zhou, G. Han, S. Tan, Z. Xie, Y. Yi, N. Li, F. Liu, J. M. Hodgkiss, C. J. Brabec and Y. Sun, *Nat. Commun.*, 2020, **11**, 6005.
6 Y. Firdaus, V. M. Le Corre, S. Karuthedath, W. Liu, A. Markina, W. Huang, S. Chattopadhyay, M. M. Nahid, M. I. Nugraha, Y. Lin, A. Seitkhan, A. Basu, W. Zhang, I. McCulloch, H. Ade, J. Labram, F. Laquai, D. Andrienko, L. J. A. Koster and T. D. Anthopoulos, *Nat. Commun.*, 2020, **11**, 5220.
7 M. T. Sajjad, A. Ruseckas, L. K. Jagadamma, Y. Zhang and I. D. W. Samuel, *J. Mater. Chem. A*, 2020, **8**, 15687–15694.
8 O. V. Mikhnenko, P. W. M. Blom and T.-Q. Nguyen, *Energy Environ. Sci.*, 2015, **8**, 1867–1888.
9 S. M. Menke and R. J. Holmes, *Energy Environ. Sci.*, 2014, **7**, 499–512.
10 D. B. Riley, P. Meredith and A. Armin, *Nanoscale*, 2024, **16**, 17761–17777.
11 Y. Shi, Y. Chang, K. Lu, Z. Chen, J. Zhang, Y. Yan, D. Qiu, Y. Liu, M. A. Adil, W. Ma, X. Hao, L. Zhu and Z. Wei, *Nat. Commun.*, 2022, **13**, 3256.
12 D. Yuan, M. A. Awais, V. Sharapov, X. Liu, A. Neshchadin, W. Chen and L. Yu, *J. Am. Chem. Soc.*, 2021, **143**, 5239–5246.
13 C. O. Diarra, M. Boero, E. Steveler, T. Heiser and E. Martin, *Phys. Chem. Chem. Phys.*, 2023, **25**, 15539–15546.
14 A. Carreras and D. Casanova, *J. Chem. Phys.*, 2022, **156**, 04411201–04411210.
15 P. Ghosh, A. M. Alvertis, R. Chowdhury, P. Murto, A. J. Gillett, S. Dong, A. J. Sneyd, H.-H. Cho, E. W. Evans, B. Monserrat, F. Li, C. Schnedermann, H. Bronstein, R. H. Friend and A. Rao, *Nature*, 2024, **629**, 355–362.
16 J. Jing, B. Heinrich, A. Prel, E. Steveler, T. Han, I. Bulut, S. Méry, Y. Leroy, N. Leclerc, P. Lévêque, M. Rosenthal, D. A. Ivanov and T. Heiser, *J. Mater. Chem. A*, 2021, **9**, 24315–24324.
17 T. Han, I. Bulut, S. Méry, B. Heinrich, P. Lévêque, N. Leclerc and T. Heiser, *J. Mater. Chem. C*, 2017, **5**, 10794–10800.
18 J. Jing, E. Steveler, N. Leclerc, A. D'Aléo, B. Heinrich, W. Uhring and T. Heiser, *Exciton Lifetime in Donor-Acceptor-Donor Planar Dumbbell-Shaped Triazatruxene-Thienopyrroledione Derivatives*, SPIE, 2022.
19 B. Ferreira, P. F. da Silva, J. S. Seixas de Melo, J. Pina and A. Maçanita, *J. Phys. Chem. B*, 2012, **116**, 2347–2355.
20 J. D. A. Lin, O. V. Mikhnenko, J. Chen, Z. Masri, A. Ruseckas, A. Mikhailovsky, R. P. Raab, J. Liu, P. W. M. Blom, M. A. Loi, C. J. García-Cervera, I. D. W. Samuel and T.-Q. Nguyen, *Mater. Horiz.*, 2014, **1**, 280–285.
21 M. T. Sajjad, O. Blaszczyk, L. K. Jagadamma, T. J. Roland, M. Chowdhury, A. Ruseckas and I. D. W. Samuel, *J. Mater. Chem. A*, 2018, **6**, 9445–9450.
22 U. Gösele, M. Hauser, U. K. A. Klein and R. Frey, *Chem. Phys. Lett.*, 1975, **34**, 519–522.
23 R. C. Powell and Z. G. Soos, *J. Lumin.*, 1975, **11**, 1–45.
24 Y. Long, G. J. Hedley, A. Ruseckas, M. Chowdhury, T. Roland, L. A. Serrano, G. Cooke and I. D. W. Samuel, *ACS Appl. Mater. Interfaces*, 2017, **9**, 14945–14952.
25 S. Chandrabose, K. Chen, A. J. Barker, J. J. Sutton, S. K. K. Prasad, J. Zhu, J. Zhou, K. C. Gordon, Z. Xie, X. Zhan and J. M. Hodgkiss, *J. Am. Chem. Soc.*, 2019, **141**, 6922–6929.
26 A. M. Gharbi, D. S. Biswas, O. Crégut, P. Malý, P. Didier, A. Klymchenko and J. Léonard, *Nanoscale*, 2024, **16**, 11550–11563.
27 S. Chandrasekhar, *Rev. Mod. Phys.*, 1943, **15**, 1–89.
28 S. M. Menke, W. A. Luhman and R. J. Holmes, *Nat. Mater.*, 2013, **12**, 152–157.
29 B. W. van der Meer, in *FRET – Förster Resonance Energy Transfer*, 2013, pp. 23–62.
30 S. Marbach, R. Claveau, F. Wang, J. Schiffler, P. Montgomery and M. Flury, *Opt. Lett.*, 2021, **46**, 809–812.
31 G. J. Krüger, *Phys. Rep.*, 1982, **82**, 229–269.
32 K. R. M. Daoud, M. Gharbia and A. Gharbi, *Braz. J. Phys.*, 1998, 28.
33 W.-Q. Deng and W. A. Goddard, *J. Phys. Chem. B*, 2004, **108**, 8614–8621.
34 Z. Li and G. Lu, *J. Phys.: Condens. Matter*, 2014, **26**, 185006–1850015.
35 S. Marbach, C. Cordier, R. Claveau, T. Engel, P. Montgomery and M. Flury, *Optics and Photonics for Advanced Dimensional Metrology*, 2020, vol. 11352, pp. 277–284.